

Entropy-driven entanglement forging

A. Pérez-Obiol,^{1,*} S. Masot-Llima,^{2,†} A. M. Romero,^{3,4,‡}
 J. Menéndez,^{3,4,§} A. Rios,^{3,4,¶} A. García-Sáez,^{2,5,**} and B. Juliá-Díaz^{3,4,††}

¹*Departament de Física, Universitat Autònoma de Barcelona, 08193 Bellaterra, Spain*

²*Barcelona Supercomputing Center, 08034 Barcelona, Spain*

³*Departament de Física Quàntica i Astrofísica, Universitat de Barcelona, 08028 Barcelona, Spain*

⁴*Institut de Ciències del Cosmos, Universitat de Barcelona, 08028 Barcelona, Spain*

⁵*Qilimanjaro Quantum Tech, 08019 Barcelona, Spain*

(Dated: Received: September 10, 2024 / Revised version: date)

Simulating a physical system with variational quantum algorithms is a well-studied approach but challenging to implement in current devices due to demands in qubit number and circuit depth. We show how limited knowledge of the system, namely the entropy of its subsystems or its entanglement structure, can be used to reduce the cost of these algorithms with entanglement forging. To do so, we simulate a Fermi-Hubbard one-dimensional chain with a parametrized hopping term, as well as atomic nuclei ²⁸Ne and ⁶⁰Ti with the nuclear shell model. Using an adaptive variational quantum eigensolver we find significant reductions in both the maximum number of qubits (up to one fourth) and the amount of two-qubit gates (over an order of magnitude) required in the quantum circuits. Our findings indicate that our method, entropy-driven entanglement forging, can be used to adjust quantum simulations to the limitations of current noisy intermediate-scale quantum devices.

I. INTRODUCTION

In modern quantum devices, the number of available qubits and low-error quantum gates imposes a strong limitation in the accuracy of the final results not only in fault-tolerant schemes but also in current noisy simulations. Since quantum algorithms are applied to complex quantum many-body problems [1, 2], including quantum chemistry [3–5], condensed matter [6, 7] and nuclear physics [8–10], this constraint has been the source of many techniques that aim to simulate large systems with smaller but equivalent ones needing fewer quantum resources. Some encoding methods aim to reduce the dimension of the input data, like quantum autoencoding [11] or other physically-inspired frameworks [12]. On the other hand, other approaches focus directly on circuits to run equivalent simulations using fewer qubits. The best-known of them, circuit knitting [13, 14], takes advantage of circuits with sparsely-connected subsections in order to break them apart into smaller ones. More recently, an alternative approach has also been explored: one can train small circuits to prepare local states, and then recover the global solution with post-processing. Both types of techniques are commonly used on variational quantum algorithms (VQA) [1, 2].

Entanglement forging [15] is an example of the latter approach. However, a challenge faced by this framework is to find which terms and corresponding weights

are more relevant in the entanglement-forging decomposition. Recently, a solution was proposed using a generative neural network [16]. Instead, in this work we argue in favour of a physically-motivated approach. In particular, we aim to exploit information about the entanglement structure of the target system [17] or, more generally, the entropy of its subsystems. These properties can indicate how to apply the decomposition and even guide the weight distribution of the product states.

We call this novel approach Entropy-Driven Entanglement Forging (EDEF). Figure 1 illustrates the EDEF algorithm, which can be applied to a physical system (middle panel) that, once encoded into qubits, can be solved with a VQA (left panel). When two low-entanglement subsystems A and B can be identified, they define a bipartition of the system where entanglement forging can be applied efficiently (right panel). In this alternative approach, the VQA is simplified into smaller circuits with fewer qubits that output local states on each subsystem after optimization. Finally, we recover the ground state of the entire system with a linear combination of the local states.

We showcase our proposal studying two many-body systems. First, we describe the one-dimensional (1D) Fermi-Hubbard (FH) model. Here we explore the performance of the EDEF algorithm across a wide range of values for the different parameters of the Hamiltonian, which lets us identify partitions with different levels of entropy. Second, we simulate the ground states of atomic nuclei using the nuclear shell model (NSM). This approach has already been the subject of several works using quantum computing tools [16, 18–24], which point out the need for a significant amount of quantum-computing resources to simulate medium-mass nuclei [24, 25]. For both systems, we implement EDEF onto an Adaptive Derivative-Assembled Pseudo-Trotter ansatz-Variational Quantum Eigensolver (ADAPT-VQE), which has previ-

* corresponding author, axel.perezobiol@uab.cat

† sergi.masot@bsc.es

‡ antonio.marquezromero@fujitsu.com

§ menendez@fqa.ub.edu

¶ arnau.rios@fqa.ub.edu

** artur.garcia@bsc.es

†† bruno@fqa.ub.edu

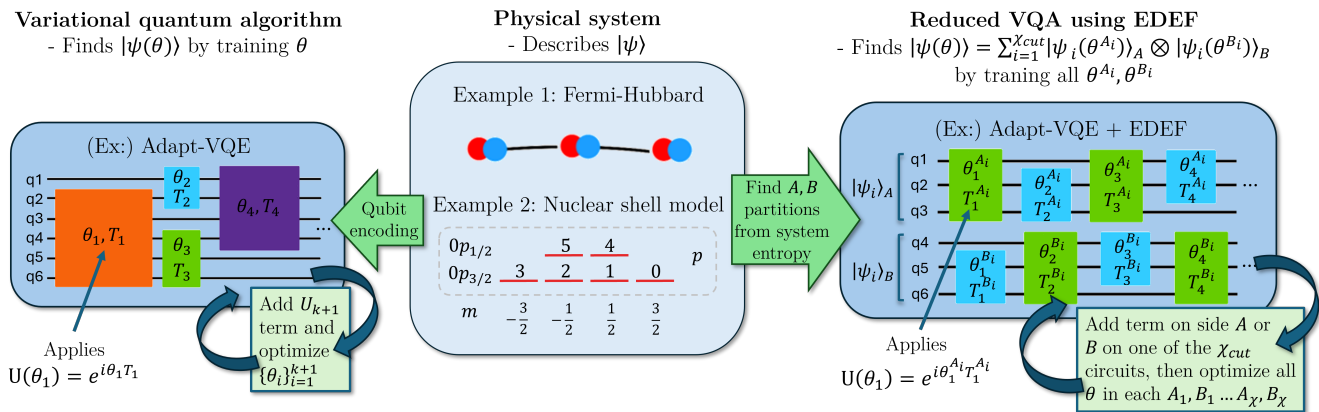


FIG. 1. Schematic application of the Entropy-Driven Entanglement Forging (EDEF) method to two physical systems: the Fermi-Hubbard and the nuclear shell model. In the middle, the initial configuration is encoded into a qubit quantum state. Then –left panel– a variational quantum algorithm (VQA) can be used to obtain the system’s ground-state by optimizing the ansatz parameters. Alternatively (right panel) the VQA is used with EDEF: knowledge of the entropy of the system is used to find a suitable partition, and thus the ground state is obtained with a few smaller circuits instead of a single large circuit.

ously shown to be effective both for the FH model [26] and the NSM [7, 18]. Nonetheless, our approach can be integrated with other VQAs in a straightforward way. As illustrated in Fig. 1, we expect that the EDEF algorithm allows us to reduce both the number of qubits and the depth of the circuits of our FH and NSM many-body simulations.

II. ENTANGLEMENT PATTERNS AND PHYSICAL MODELS

A. Entropy-driven entanglement forging

For any possible bipartition of a quantum system, bipartite entanglement [27] quantifies how correlated the two parts are – albeit with some subtleties that distinguish quantum effects from classical correlations [28]. In a pure quantum state, $|\psi\rangle$, with density matrix, $\rho = |\psi\rangle\langle\psi|$, subsystems A and B of ρ are not entangled when they can be written down as a tensor product, $\rho = \rho_A \otimes \rho_B$. Otherwise, one can use the von Neumann entropy, S , defined as

$$S(\rho) = -\text{Tr}(\rho \log_2 \rho) = -\sum_i \rho_i \log_2 \rho_i, \quad (1)$$

where ρ_i are the eigenvalues of ρ . Specifically, for a pure state, $S(|\psi\rangle\langle\psi|) = 0$, while for a reduced matrix $\rho_A = \text{tr}_B(\rho)$, $S(\rho_A) = S(\rho_B) = S(\text{tr}_A(\rho))$ quantifies the entanglement between A and B .

The Schmidt decomposition of a quantum state [29] for the same bipartition A, B ,

$$|\psi\rangle = \sum_i^\chi \lambda_i |\psi_i\rangle_A \otimes |\psi_i\rangle_B, \quad (2)$$

is useful to calculate the entropy because $\rho_i = \lambda_i^2$. More importantly, it also describes exactly how to assemble in entanglement forging the subcircuits that describe the two parts, $|\psi_i\rangle_A$ and $|\psi_i\rangle_B$, into the full state, $|\psi\rangle$. For an exact simulation, the amount of subcircuits needed corresponds to the Schmidt number χ , which is bound by the amount of basis elements in the smallest partition. On the other hand, χ is the number of terms in the sum of Eq. (1), which maximizes the entropy when all ρ_i are equal and $\text{Tr}(\rho) = 1$, with $S = \log_2(\chi)$. Therefore, for an equipartite N_q -qubit system such as the ones we consider in this work, we have

$$2^S \leq \chi \leq 2^{N_q/2}. \quad (3)$$

Quantum systems that are fully separable on a bipartition only need one state for each part, therefore, entanglement forging is simplest for these systems. For low entanglement between the two parts, only a few instances χ_{cut} of each subsystem are necessary to simulate it accurately, since there is a tail of terms with very small coefficients λ_i that contribute negligibly to the fidelity. In contrast, for strongly-entangled subsystems one needs exponentially many states with the smallest number of qubits in one of the subsystems. Thus, in a general setting of entanglement forging, one must find a favourable bipartition, decide how many subcircuits to run, and optimize the coefficients for each of them to recover the full quantum state. Since the number of possible bipartitions in a system scales exponentially with the number of qubits N_q , entanglement forging is best suited when it is physically driven, for instance when knowledge of the system indicates low entanglement across specific sectors.

In this work, we illustrate EDEF by studying the 1D FH model with a tunable hopping term between the two central sites. This model allows us to test different levels of entropy and their impact on the quality of the results after applying one layer of EDEF. In addition, the low

entanglement present between the protons and neutrons of atomic nuclei studied with the NSM [30, 31] provides an ideal practical testbed for EDEF. While we focus on the ADAPT-VQE algorithm, other VQAs can also be applied to the local circuits.

For a general physical system, we define Entropy-Driven Entanglement Forging as the following algorithm:

Algorithm Entropy-Driven Entanglement Forging

- 1: **procedure** PREPARATION
 - 2: **for** each of l layers of EDEF **do**
 - 3: Identify low entropy bipartition A, B
 - 4: Define initial basis of states $|\psi_i^0\rangle_A, |\psi_i^0\rangle_B$
 - 5: Tie degenerate coefficients λ_i using symmetry
 - 6: Set cutoff number of product states χ_{cut}
 - 7: **procedure** TRAINING
 - 8: Define state $|\psi\rangle = \sum_i^{\chi_{cut}} \lambda_i |\psi_i^0\rangle_A \otimes |\psi_i^0\rangle_B$
 - 9: **while** $\varepsilon' > \text{threshold}$ **do**
 - 10: Optimize $\mathcal{U}_A^i(\theta), \mathcal{U}_B^i(\theta)$ independently on circ. i
 - 11: Compute $\mathcal{U}_A \otimes \mathcal{U}_B \rightarrow \mathcal{U}_{VQA}$
 - 12: Compute $\varepsilon'(\mathcal{U}_{VQA}, |\psi\rangle)$
-

In this pseudocode, A, B denote the two partitions of the system, the unitaries $\mathcal{U}_A^i, \mathcal{U}_B^i$ are applied individually to circuit i of the decomposition on the corresponding partition, and ε' is the ground-state energy found with EDEF. The bases in the fourth step must have well-defined quantum numbers according to the model Hamiltonian and the partition. Throughout this work, we refer to the application of l layers of EDEF as l -cut EDEF.

B. Fermi-Hubbard model

The Fermi-Hubbard model describes fermions on a lattice and serves as a simplified model to simulate valence electrons on a crystal and fermionic ultracold gases in optical lattices [32]. In its simplest 1D form, the FH Hamiltonian includes a hopping term, t , accounting for the tunneling of fermions between adjacent sites, and an interaction term, U , which adds energy whenever a spin-up and a spin-down fermion occupy the same site. Here we consider a 1D lattice with an even number of sites, labeled $i = 1, \dots, N_s$, and a tunable hopping, t_m , between the two middle sites: $i = N_s/2, N_s/2 + 1$. The Hamiltonian reads,

$$H_0 = -t \sum_{\langle i, j \rangle, \sigma} \left(a_{i\sigma}^\dagger a_{j\sigma} + a_{j\sigma}^\dagger a_{i\sigma} \right) + U \sum_i n_{i\uparrow} n_{i\downarrow} - (t_m - t) \sum_{\sigma} \left(a_{i_m\sigma}^\dagger a_{j_m\sigma} + a_{j_m\sigma}^\dagger a_{i_m\sigma} \right), \quad (4)$$

where $a_{j_m\sigma}$ ($a_{j_m\sigma}^\dagger$) are the annihilation (creation) operators for a fermion at site j and spin σ , with $j = 1, \dots, N_s$ and $\sigma = \uparrow, \downarrow$; $n_{i\sigma} = a_{i\sigma}^\dagger a_{i\sigma}$ is the number operator, while $\langle i, j \rangle$ indicates pairs of first-neighbor sites, and $i_m = N_s/2, j_m = i_m + 1$ the two middle sites. We

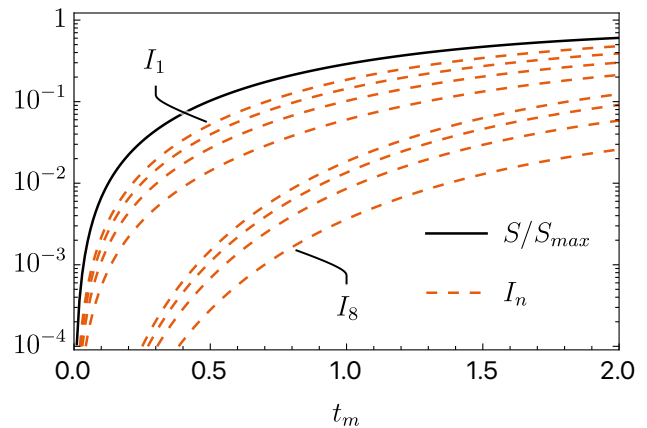


FIG. 2. Normalized entropy S/S_{max} (black solid line) and infidelities I_n corresponding to normalized Schmidt decompositions with $n = 1, \dots, 8$ product states (red dashed lines, from top to bottom) as a function of the hopping t_m between the two middle sites for a FH model with four sites and $t = U$.

consider repulsive interactions, $U > 0$, with $t > 0$, $t_m > 0$. Here, we set t as our energy unit and vary t_m and U , while fixing the number of particles for each spin, N_σ . The regular FH Hamiltonian corresponds to $t_m = t$, while smaller (larger) values of t_m couple more weakly (strongly) the left and right parts of the lattice, thus reducing (enhancing) their entanglement. In a standard Jordan-Wigner mapping [33] with $N_q = 2N_s$ qubits where odd ones ($i = 1, \dots, 2N_s - 1$) correspond to spin-up sites and even qubits ($i = 2, \dots, 2N_s$) to spin-down sites, the entanglement is given by the von Neumann entropy in Eq. (1), S , between the first and second halves of qubits. Following Eq. (3), the entropy is upper bounded by $S_{max} = N_s$. Figure 2 shows S/S_{max} as a function of t_m for a lattice with $N_s = 4$ sites, $U = t$, and half-filling, $N_\uparrow = N_\downarrow = 2$. The entropy at $t_m = 0$ vanishes as the Hamiltonian can be written as a tensor product of two parts involving only the left or right $N_s/2$ sites. As t_m increases, the entropy grows up to $S/S_{max} = 0.60$ at $t_m = 2t$. For larger t_m (not shown in Fig. 2), the entropy keeps growing and then slightly decreases, converging to $S/S_{max} = 0.75$ as $t_m \rightarrow \infty$.

The entropy can also be written in terms of Schmidt coefficients λ_i as in Eq. (2),

$$S = - \sum_i \lambda_i^2 \log_2(\lambda_i^2). \quad (5)$$

Related to this expression, we can compute the infidelity, I_n , of a Schmidt decomposition cut off at the n -th singular value and normalized to one, $|\psi_n\rangle$, when compared to the exact ground state, $|\psi_\chi\rangle$,

$$I_n = 1 - |\langle \psi_\chi | \psi_n \rangle|^2 = 1 - \sum_i^n \lambda_i^2. \quad (6)$$

I_n always decreases for larger n , as the singular values λ_i^2 are non-negative real numbers sorted in decreasing or-

der. Figure 2 also shows the infidelities for $n = 1, \dots, 8$ (dashed red lines) as a function of t_m , for the FH model described in the above paragraph. For $t_m = 0$, there is only one singular value $\lambda_1 = 1$ and all $I_n = 0$. As t_m increases, the I_n 's grow at different rates. This indicates that depending on the target infidelity and t_m value, a different cutoff n will be needed, and if I_n is good enough for our purpose, then EDEF with $\chi_{cut} = n$ provides a suitable approximation. Nonetheless, the large gap between I_4 and I_5 for middle hoppings $t_m \lesssim t$, makes $n = 5$ a particularly efficient cutoff.

This feature can be understood by the spin and parity symmetries of the FH Hamiltonian: Eq. (4) is invariant under the exchange of spin-up and spin-down operators, $\sigma \leftrightarrow \bar{\sigma}$, and under exchanging each operator acting on site i by its mirror operator, $i \leftrightarrow N_s + 1 - i$. Therefore, product states in the Schmidt decomposition related by these transformations have degenerate singular values. Figure 3 illustrates this degeneracy by showing the first eight singular values for three different middle hopping values, $t_m = t/2, t, 2t$, and two different interactions, $U = t, 3t$. In all cases, a first large, non-degenerate, singular value is followed by four small degenerate ones, while the sixth singular value is very suppressed. The first singular value corresponds to an even distribution of particles and spins between the left and right partitions, labeled $(\uparrow\downarrow, \uparrow\downarrow)$. For this symmetric distribution the interactions minimize double occupation of the same site, and the hopping term delocalizes fermions. The next four degenerate singular values correspond to the partitions related by spin and parity transformations: $(\uparrow\uparrow\downarrow, \downarrow)$, $(\downarrow, \uparrow\uparrow\downarrow)$, $(\downarrow\downarrow\uparrow, \uparrow)$, and $(\uparrow, \downarrow\downarrow\uparrow)$. Thus, the gap between I_4 and I_5 in Fig. 2 appears because once the fifth product state is added, the sum of singular values suddenly approaches 1, suppressing the infidelity. The following singular values are much smaller making the corresponding infidelities relatively close to I_5 . This feature is more prominent as t_m decreases, so that a weaker central hopping makes the $n = 5$ cutoff more efficient. Interactions U do not change notably the singular-value structure.

In the following, we fix the number of sites to $N_s = 4$ and use the same set of central hopping terms t_m and interactions U of Fig. 3 to illustrate the performance of EDEF in different settings. Nonetheless, the distribution of spin-up and spin-down fermions discussed in this section, N_\uparrow and N_\downarrow , generalizes to lattices with more sites (eg $N_s = 6, N_s = 8$) and particles, as long as interactions U are not large (eg $U = t$) and $N_\uparrow = N_\downarrow$ is even. In these cases, the first product state consists of $N_\uparrow/2$ and $N_\downarrow/2$ in each side, while the following four product states are four-fold degenerate, corresponding to $N_\uparrow/2 - 1$ and $N_\downarrow/2 + 1$ on the left, and the corresponding degenerate product states obtained by left/right and spin-up/spin-down exchanges.

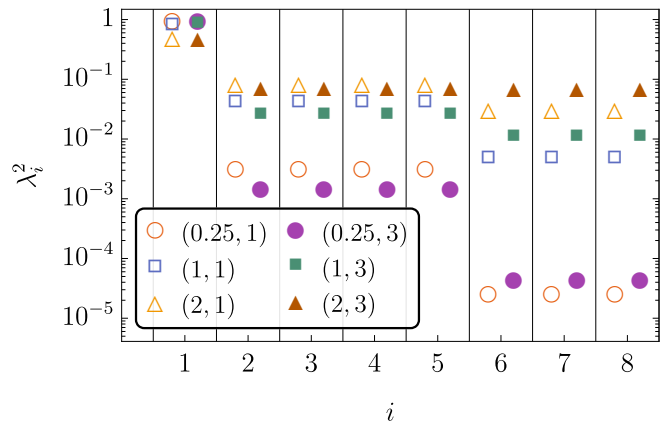


FIG. 3. First eight singular values, λ_i , of the Schmidt decomposition into left and right sites of the ground state of the FH model with 4 particles, for different interaction strengths, U , and central hopping terms, t_m , labeled as (t_m, U) . Empty (solid) symbols indicate $U = t$ ($U = 3t$) singular values. As the central hopping is reduced, the values $i \geq 2$ get smaller.

C. Nuclear shell model

The nuclear shell model (NSM), or configuration-interaction method, is one of the most successful frameworks to study nuclear structure [34–39]. Much alike its atomic counterpart, the NSM characterizes nuclear dynamics in a restricted configuration space, also called valence space, where nucleons effectively interact. The valence space is bounded by single-particle states which, if completely filled with nucleons, lead to *magic numbers* that characterize especially stable configurations associated with large energy gaps. As the nuclear interaction is rotationally invariant and nucleons are fermions, the single-particle basis states are labelled by the quantum numbers pl_j and m , where p is the principal quantum number, l the orbital angular momentum – usually given in spectroscopic notation – and j the total angular momentum with third-component projection m . As illustrated in Fig. 4, single-particle states with the same pl_j and different m are degenerate in energy. The effective Hamiltonian in the valence space is

$$H_{\text{eff}} = \sum_i \varepsilon_i a_i^\dagger a_i + \frac{1}{4} \sum_{ijkl} \bar{v}_{ijkl} a_i^\dagger a_j^\dagger a_l a_k, \quad (7)$$

where a_i (a_i^\dagger) annihilate (create) a nucleon in the single-particle state i with energy ε_i . The antisymmetrized two-body matrix elements $\bar{v}_{ijkl} = v_{ijkl} - v_{ijlk}$ are obtained from the full-space nucleon-nucleon interaction. In this work, we use the standard USDB interaction [40] in the *sd* shell for neon, and KB3G [41] in the *pf* shell for titanium. Figure 4 shows the orbitals comprising these valence spaces: $0d_{5/2}$, $1s_{1/2}$ and $0d_{3/2}$ for the *sd* shell and $0f_{7/2}$, $1p_{3/2}$, $1p_{1/2}$ and $0f_{5/2}$ for the *pf* shell, ordered according to their single-particle energy.

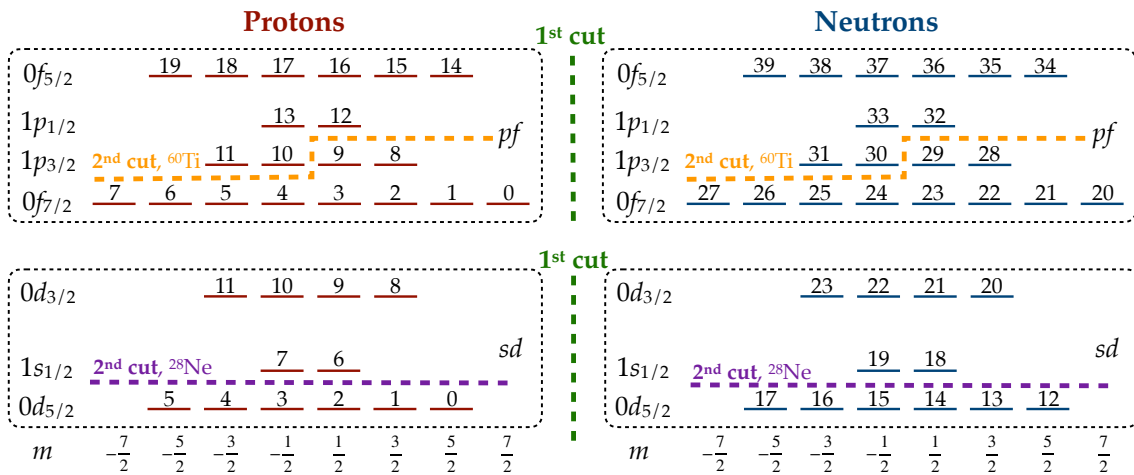


FIG. 4. Partitions used in the first and second layers of EDEF (labelled as 1st and 2nd cut) for the nuclear shell model in the *sd* and *pf* valence spaces. The number on top of each single-particle state labels the qubit for the implementation in ADAPT-VQE under a Jordan–Wigner mapping. The first cut always separates the proton and neutron sectors, while the second cut aims to separate orbitals according to their energy (orbitals are ordered by their energy, with lowest-energy ones at the bottom).

For a nucleus with Z protons and N neutrons, one can expand the nuclear states in the many-body basis of the M -scheme, or Slater determinants,

$$|JMTT_z\rangle = \sum_{\alpha} a_{\alpha} |\alpha; MT_z\rangle, \quad (8)$$

where M is the projection of the total angular momentum of the nucleus, J , and $T_z = (N - Z)/2$ the one of the total nuclear isospin, T . The coefficients a_{α} are obtained by diagonalizing the Hamiltonian in the many-body basis and guarantee that nuclear states have good J and T quantum numbers. State-of-the-art nuclear shell-model codes [42–45] face the challenge to build and diagonalize the Hamiltonian matrix for heavy nuclei. This is because the many-body basis, formed by the exponentially-growing set of all possible configurations for protons and neutrons in the valence space, becomes untractable for classical computers when nucleons fill about half the valence-space single-particle states.

In the advent of quantum computers, alternative quantum algorithms have been proposed to find ground states within the NSM [16, 18–25]. In parallel, recent works provide nuclear structure insights by analyzing nuclei in terms of quantum information measures such as the von Neumann entropy [20, 46–50]. Notably, among all possible bipartitions, separating proton and neutron orbitals has the lowest von Neumann entropy [31], and proton-neutron entanglement decreases further for more neutron-rich systems [30]. In fact, these properties have been used to improve nuclear-structure calculations using classical methods [51, 52].

Here we apply these insights into the Schmidt decomposition of Eq. (2). Figure 5 shows the first eight singular values for various beryllium (calculated with the Cohen-Kurath interaction [53] in the $0p_{3/2}, 0p_{1/2}$ valence space),

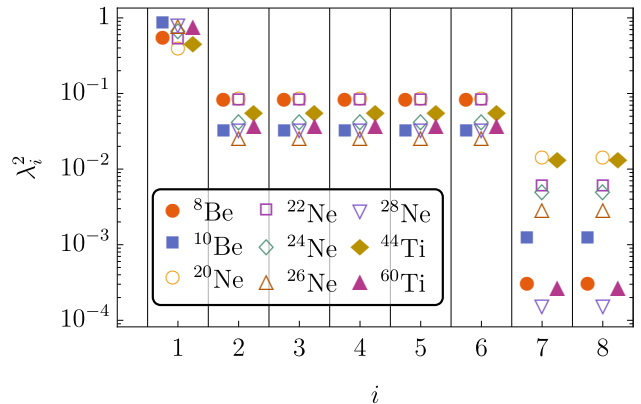


FIG. 5. First eight singular values, λ_i , of the Schmidt decomposition of into protons and neutrons for the NSM ground state of various beryllium (*p* shell), neon (*sd* shell) and titanium (*pf* shell) nuclei. In all cases a first large singular value is followed by much smaller five-fold degenerate second to seventh singular values, specially for neutron-rich isotopes.

neon, and titanium isotopes. In all nuclei, the singular values become smaller exponentially, especially for the most neutron-rich nuclei ^{28}Ne and ^{60}Ti , and consist of a first large non-degenerate value followed by five degenerate ones. This degeneracy can be associated with five product states with opposite M in the proton and neutron states, denoted $|M^{(p)}\rangle \otimes |M^{(n)}\rangle$: $|\pm 2\rangle \otimes |\mp 2\rangle$, $|\pm 1\rangle \otimes |\mp 1\rangle$, and $|0\rangle \otimes |0\rangle$. These results suggests that nuclear ground states, especially for neutron-rich nuclei, can be well approximated within six separate product states of only protons and neutrons. Due to degeneracy and normalization, just a single coefficient is needed.

In addition, nuclear entanglement can also be partly understood in terms of subshell closures and occupation

numbers. Nuclei with proton or neutron orbitals mostly empty or fully-occupied present very low entanglement of these orbitals with the rest. This feature motivates to apply entanglement forging in an iterative fashion: firstly, using a proton-neutron partition; and secondly using an energy-based subpartition, separating the higher- and lower-energy single-particle states for each proton and neutron subsystem. Figure 4 illustrates the two partitions and the corresponding cuts used for ^{28}Ne and ^{60}Ti . For the latter nucleus, a bipartition into subsystems of the same size requires separating the energy-degenerate single-particle states of the $1p_{3/2}$ orbital.

III. ENTROPY-DRIVEN ENTANGLEMENT FORGING WITH ADAPT-VQE

ADAPT-VQE [54–58] is a variational quantum algorithm which updates iteratively a user-defined ansatz, rather than optimizing a fixed number of parameters as the UCC-VQE [3, 19, 20]. Each iteration k adds a new unitary operator, $A_k = e^{i\theta_k T_k}$, to the ansatz, with a new parameter, θ_k , and a hermitian operator from a predefined pool, T_k . Then, all parameters, $\boldsymbol{\theta} = \{\theta_1, \dots, \theta_k\}$, are optimized simultaneously to minimize the energy,

$$E_{\text{ADAPT-VQE}} = \min_{\boldsymbol{\theta}} \frac{\langle \psi(\boldsymbol{\theta}) | H_{\text{eff}} | \psi(\boldsymbol{\theta}) \rangle}{\langle \psi(\boldsymbol{\theta}) | \psi(\boldsymbol{\theta}) \rangle}. \quad (9)$$

This optimization starts with the values for $\theta_1, \dots, \theta_{k-1}$ from the minimization of the previous $k-1$ iteration and $\theta_k = 0$. The operator T_k is chosen such that the energy gradient with respect to θ_k ,

$$\left. \frac{\partial E^{(n)}}{\partial \theta_k} \right|_{\theta_k=0} = i \langle \psi(\boldsymbol{\theta}) | [H_{\text{eff}}, A_k] | \psi(\boldsymbol{\theta}) \rangle \Big|_{\theta_k=0}, \quad (10)$$

is maximum. Thus, by starting from the minimum in the $(k-1)$ -dimensional parameter space and maximizing the gradient in the new dimension, the algorithm gradually increases the parameter space while always decreasing the energy. ADAPT-VQE was originally proposed to solve the electronic structure of the ground state of molecules [59, 60], and since then it has been applied to a broad variety of quantum many-body systems, including lattice quantum chromodynamics [61, 62], the NSM [18, 25], algebraic nuclear models [18, 63] and nuclear pairing [64]. In addition to the novel FH simulations, we build on our previous work [25, 31] and optimize the ADAPT-VQE algorithm to solve NSM ground states with fewer quantum resources by using EDEF.

ADAPT-VQE requires a choice of reference state and a pool of operators. For the latter, we take all the two-body hopping operators,

$$T_{rs}^{pq} = i(a_p^\dagger a_q^\dagger a_r a_s - a_r^\dagger a_s^\dagger a_p a_q), \quad (11)$$

with the restriction that they conserve the Hamiltonian symmetries: the spin for the FH and M, T_z for the NSM.

For the FH, in addition, we also include one-body operators,

$$T_s^r = i(a_r^\dagger a_s - a_s^\dagger a_r). \quad (12)$$

As a reference state, with the standard ADAPT-VQE we choose the lowest-energy Slater determinant in the Fock basis of the particular FH lattice or nucleus, as it can be implemented with only one-qubit gates with the Jordan-Wigner mapping. With EDEF, however, we can exploit other physical arguments, for example the degeneracies in the Schmidt decomposition. In the case of the FH model, the best choice is a symmetric distribution of up and down spins between the left (l) and right (r) parts of the lattice:

$$|\psi\rangle = \lambda_0 |l_{\uparrow\downarrow}\rangle \otimes |r_{\uparrow\downarrow}\rangle + \lambda_1 \left(|l_{\uparrow\uparrow\downarrow}\rangle \otimes |r_{\downarrow}\rangle + |l_{\downarrow}\rangle \otimes |r_{\uparrow\uparrow\downarrow}\rangle + |l_{\uparrow\downarrow\downarrow}\rangle \otimes |r_{\uparrow}\rangle + |l_{\uparrow}\rangle \otimes |r_{\uparrow\downarrow\downarrow}\rangle \right). \quad (13)$$

In turn, for the NSM we use eigenstates of the J_z operator in the proton (p_M) and neutron (n_M) sectors, with the pattern described in Sec. II C,

$$|\psi\rangle = \lambda_0 |\tilde{p}_0\rangle \otimes |\tilde{n}_0\rangle + \lambda_1 \left(|p_{-2}\rangle \otimes |n_2\rangle + |p_{-1}\rangle \otimes |n_1\rangle + |p_0\rangle \otimes |n_0\rangle + |p_1\rangle \otimes |n_{-1}\rangle + |p_2\rangle \otimes |n_{-2}\rangle \right). \quad (14)$$

The operator pool preserves the quantum numbers for each subsystem. In order to ensure orthogonality in the NSM when $M^{(p)}$ and $M^{(n)}$ are common, we start from two orthogonal Slater determinants and use the same choice of operators for both states. The second layer of EDEF splits the proton (neutron) nuclear ground state into symmetric distributions of protons (neutrons) and proton holes (neutron holes). Appendix A gives further details on the properties of these states and their corresponding coefficients, illustrated with examples.

IV. RESULTS USING ENTROPY-DRIVEN ENTANGLEMENT FORGING

A. Fermi-Hubbard model

In the FH model we can study systems with a wide range of entanglement and analyze the impact of the EDEF method. For this purpose, like in Sec. II B and Fig. 3, we simulate systems with three different central hopping values, $t_m = 0.25t, t, 2t$, and two interactions, $U = t, 3t$. We obtain the ground state of these systems using two methods: the regular ADAPT-VQE and an optimized version using EDEF, as described in Sec. III. For their comparison, we focus on the infidelities of each approach with respect to the exact ground state,

$$I = 1 - |\langle \psi_{\text{ADAPT-VQE}} | \psi_{\text{exact}} \rangle|^2. \quad (15)$$

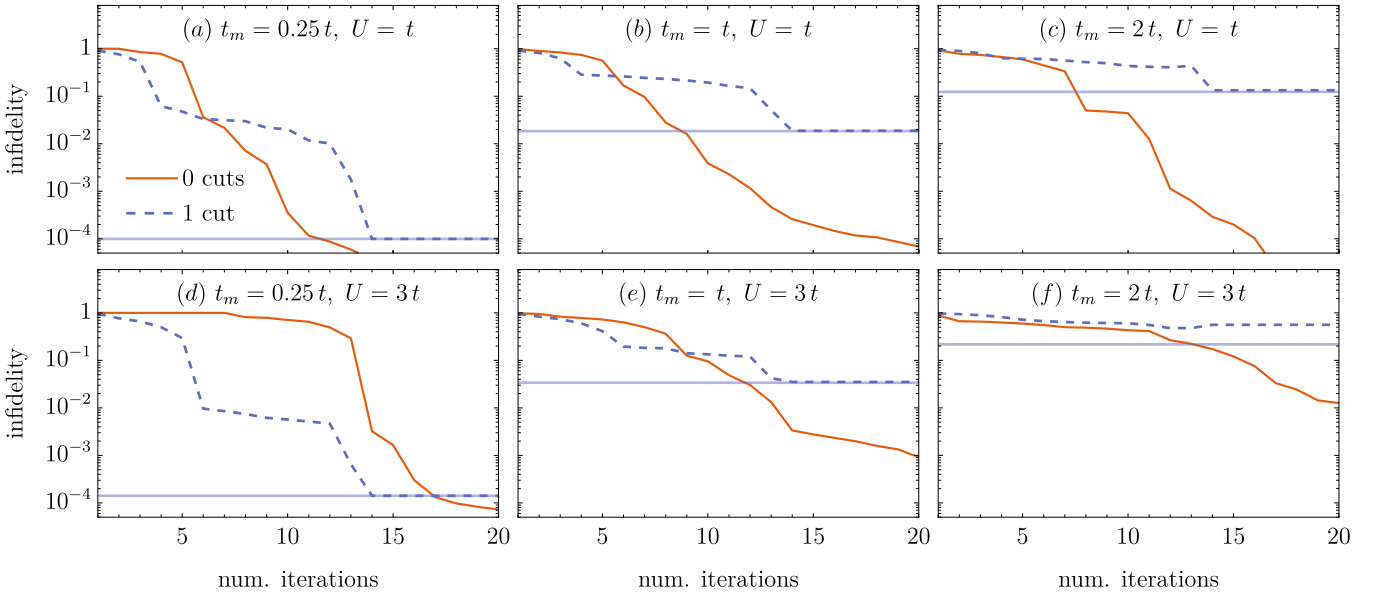


FIG. 6. Infidelity as a number of ADAPT-VQE iterations for the same FH model parameters (middle hopping t_m , interaction U) as in Fig. 3. ADAPT-VQE without entanglement forging (solid red lines) is compared with one layer of EDEF (labelled “1 cut”, dashed blue lines). Horizontal lines indicate the infidelity minimum set by the Schmidt-decomposition cutoff.

An alternative analysis of the ground-state energy relative error,

$$\epsilon_E = \left| \frac{E_{\text{ADAPT-VQE}} - E_{\text{exact}}}{E_{\text{exact}}} \right|, \quad (16)$$

gives very similar results.

Figure 6 compares the infidelities obtained with the regular ADAPT-VQE without entanglement forging (solid red line) and with EDEF with one layer, or “1-cut” (dashed blue line), keeping five singular values. The central hopping strength increases from left to right panels. Bottom panels correspond to a stronger interaction U , which causes the regular ADAPT-VQE to converge slower, but makes no difference for the 1-cut EDEF results. Horizontal lines mark the lower bound for our ansatz infidelities, given by the ones corresponding to the Schmidt decomposition of the ground state with cut-off at the fifth product state, Eq. (13). Almost all 1-cut EDEF simulations converge to this bound, highlighting the good performance of the variational optimization.

Figure 6 shows that for weakly linked FH lattices, $t_m = 0.25t$, one layer of EDEF offers a clear advantage for $U = 3t$ and target infidelities $\epsilon_E \gtrsim 10^{-4}$. For a weaker interaction $U = t$, the 1-cut EDEF infidelities also improve over regular ADAPT-VQE ones up to $I \sim 10^{-2}$ (or seven iterations). Beyond this point, ADAPT-VQE converges faster. For the canonical FH lattice, $t_m = t$, the entropy is still low – see Fig. 2 – and Fig. 6 indicates that 1-cut EDEF reaches almost $I \sim 10^{-2}$, although converging more slowly than the regular ADAPT-VQE. However, Fig. 6 shows that, when $t_m > t$, EDEF starts to fail due to the higher entropy. For these systems, reaching $I \lesssim 10^{-3}$ would require to train more than eight copies

of the circuit, which would no be a clear advantage over using all qubits like in the regular ADAPT-VQE.

Table I (top rows) quantifies the resources and performance of the FH simulations using regular ADAPT-VQE and the EDEF optimization. It lists the number of iterations, N_{it} , and the infidelity, I_{conv} , and energy relative error, ϵ_E , once the optimization has converged. Table I also presents the convergence rate, defined as

$$r \equiv \frac{-\log(I_{\text{conv}})}{N_{\text{it}}}. \quad (17)$$

Consistently with Fig. 6, the 1-cut EDEF convergence rates are higher for weaker central hopping values, but in general they are lower than for the regular ADAPT-VQE. Nonetheless, Table I also highlights that all 1-cut simulations require half the qubits and converge with just 14 iterations, while all regular ADAPT-VQE optimizations need all qubits and more iterations – but they reach $I \leq 10^{-5}$. Moreover, circuits with half as many qubits constrain fermion operators to be more local, and therefore involve fewer quantum gates, which is another advantage of the EDEF implementation.

B. Nuclear shell model

We then apply our method to study neutron-rich nuclei ^{28}Ne and ^{60}Ti withing the NSM. These are ideal systems for EDEF because of their low entanglement between neutrons and protons, as shown in Fig. 5. Also, they present a challenge for the regular ADAPT-VQE due to relatively large number of nucleons and single-particle

	cuts	N_q	N_{it}	ϵ_E	I_{conv}	r
(1,0.25)	0	8	16	7.4×10^{-6}	5.6×10^{-6}	0.74
	1	4	14	1.1×10^{-4}	9.9×10^{-5}	0.61
(1,1)	0	8	24	1.4×10^{-5}	8.0×10^{-6}	0.47
	1	4	14	1.9×10^{-2}	1.9×10^{-2}	0.26
(1,2)	0	8	19	1.6×10^{-5}	9.5×10^{-6}	0.58
	1	4	14	1.2×10^{-1}	1.3×10^{-1}	0.13
(3,0.25)	0	8	24	1.8×10^{-5}	9.4×10^{-6}	0.46
	1	4	14	1.5×10^{-4}	1.4×10^{-4}	0.59
(3,1)	0	8	31	2.0×10^{-5}	5.4×10^{-6}	0.35
	1	4	14	3.2×10^{-2}	3.5×10^{-2}	0.22
(3,2)	0	8	34	3.2×10^{-6}	3.7×10^{-6}	0.37
	1	4	14	3.8×10^{-1}	5.6×10^{-1}	0.039
^{28}Ne	0	24	100	6.2×10^{-3}	1.0×10^{-1}	0.023
	1	12	85	6.0×10^{-4}	2.9×10^{-3}	0.069
	2	6	48	9.8×10^{-3}	5.1×10^{-2}	0.062
^{60}Ti	1	12	57	1.7×10^{-1}	2.5×10^{-1}	0.024
	2	6	42	1.6×10^{-1}	8.2×10^{-2}	0.059

TABLE I. Number of qubits (N_q) per circuit used to simulate the system with regular (0 cuts) and EDEF optimized (1 or 2 cuts) ADAPT-VQE, as well as the number of iterations (N_{it}), relative error in the energy (ϵ_E), infidelity (I_{conv}) and convergence rate (r) once the algorithm has either converged ($I_{conv} < 10^{-5}$ for ADAPT-VQE) or reached the maximum number of iterations imposed. Top: Results for FH lattices labeled as (U, t_m) . Bottom: Results for the NSM simulations of ^{28}Ne and ^{60}Ti .

states involved. In fact, in our previous work [25] we were not able to simulate ^{60}Ti with ADAPT-VQE.

We explore the performance of EDEF using various layers. In particular, we use ADAPT-VQE with circuits with N_q (regular ADAPT-VQE), $N_q/2$ (EDEF with one layer), and $N_q/4$ (EDEF with two layers) qubits. As indicated in Fig. 4, N_q is the number of single-particle states in the valence space, so that $N_q = 24$ for ^{28}Ne and $N_q = 40$ for ^{60}Ti . Like in Sec. IV A, we present our results in terms of the infidelity with respect to the exact ground state obtained with each approach.

The top panel of Fig. 7 presents the ^{28}Ne infidelities as a function of the number of ADAPT-VQE iterations for the regular ADAPT-VQE (solid red line), 1-cut EDEF (dashed blue line) and 2-cut EDEF (dashed-dotted yellow line). Like for the FH model, the infidelities for one and two layers of EDEF converge very close to the lower bounds defined by the Schmidt decomposition (horizontal lines of the same color). The two EDEF variants converge faster than the regular ADAPT-VQE, meaning that with the same number of parameters, and half or one quarter of the qubits per circuit, EDEF outperforms ADAPT-VQE. The 1-cut EDEF reaches much lower infidelities, $I \sim 10^{-3}$, than the 2-cut EDEF simulation, but after significantly more iterations. Indeed, the results in Table I indicate that the convergence rate is similar in both cases.

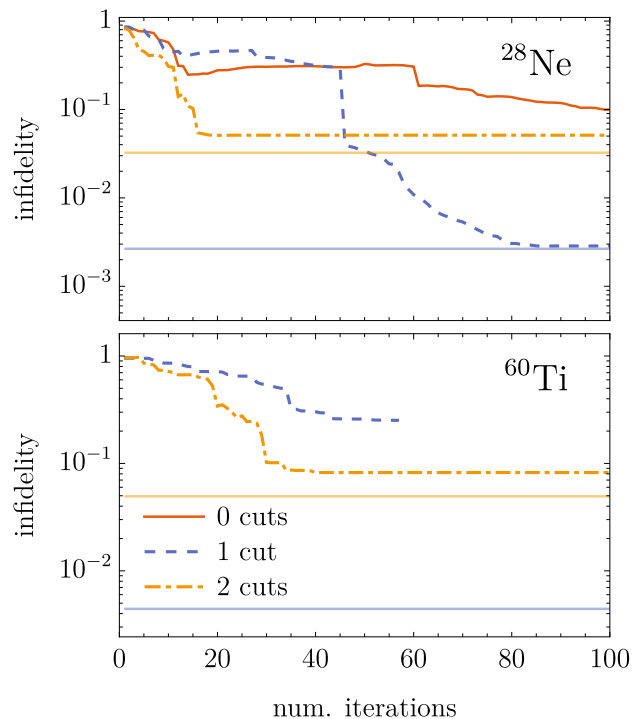


FIG. 7. Infidelities as a function of the number of ADAPT-VQE iterations for NSM simulations of ^{28}Ne (top) and ^{60}Ti (bottom), using the regular ADAPT-VQE (0 cuts, solid red line) and the optimized EDEF with one (1 cut, dashed blue lines) or two (2 cuts, dashed-dotted yellow lines) layers. Horizontal lines with the same color code indicate the infidelities set by the Schmidt decompositions cut off consistently with each EDEF simulation.

The bottom panel of Fig. 7 shows the results for ^{60}Ti with one and two layers of EDEF, with the same line and color code as the upper panel. For this nucleus, standard ADAPT-VQE with no cuts exceeds our computational capabilities. While the infidelity for 1-cut EDEF shows good convergence up to ~ 50 iterations, at this point, when I is still well above the limit set by the Schmidt decomposition, the computation becomes too slow. In contrast, the 2-cut EDEF converges to a high-quality local minimum at the 42nd iteration, with $I = 0.082$ (the relative error in the energy is $\epsilon_E = 0.16$). Consistently, Table I indicates a better convergence for the 2-cut simulation.

In principle, EDEF can also be applied to less neutron-rich nuclei, but this implies larger proton-neutron entanglement and thus reduced efficiency. For example, ^{26}Ne shows more complex structure in terms of product states than ^{28}Ne . Nonetheless, the one-layer EDEF achieves only marginally poorer infidelity and relative energy error than the regular ADAPT-VQE using half as many qubits. The results for ^{26}Ne are given in Appendix B.

C. Number of CNOT gates in EDEF NSM simulations

An important factor for the implementation of the current algorithm in quantum computers is the depth of the circuit, which is largely dependent on the number of two-qubit gates needed. This is specially relevant for NSM simulations, which already for medium-mass nuclei require a very significant amount of resources well beyond current capabilities [24, 25].

Figure 8 compares the number of CNOT gates required in the NSM simulation of ^{28}Ne and ^{60}Ti in the case of regular ADAPT-VQE and EDEF with one or two layers. Since the latter cases involve several circuits, Fig. 8 selects the one with maximum number of CNOT gates. The top panel shows that, for ^{28}Ne , the number of CNOTs in the 24-qubit circuit (ADAPT-VQE, solid red line) is drastically reduced in one order of magnitude throughout the whole optimization by EDEF with one layer using 12 qubits (1-cut EDEF, dashed blue line). The 6-qubit EDEF with two layers (2-cut EDEF, dotted-dashed yellow line) reduces the number of CNOTs in an additional order of magnitude. Consistently, the bottom panel of Fig. 8 indicates that for ^{60}Ti the number of CNOTs is smaller in the 2-cut EDEF, which uses 10-qubit circuits, than in the 1-cut EDEF involving 20 qubits. These results highlight that for these systems, our EDEF approach, in addition to having better performance than the regular ADAPT-VQE as shown in Sec. IV B, is also better suited to be implemented in near-future quantum devices.

The reason for the reduction of CNOT gates with EDEF is twofold. First, each additional EDEF cut makes circuits much shallower because at each iteration an operator is added to a single circuit, distributing the CNOT gates among all circuits rather than accumulating them in a single one. Moreover, circuits with fewer qubits constrain the fermionic operators in the ADAPT-VQE pool to be more local, requiring less CNOT gates in the Jordan-Wigner mapping.

Among EDEF circuits, both for ^{60}Ti and ^{28}Ne , the ones with most CNOT gates are those simulating the first, non-degenerate, product state in the Schmidt decomposition, $\lambda_0|\tilde{p}_0\rangle \otimes |\tilde{n}_0\rangle$ in Eq. (14). This is because the ADAPT-VQE algorithm finds, in most iterations, largest gradients for operators added to the first, $J_z = 0$ proton-neutron product state. This is expected from the Schmidt decomposition, as the first singular value is much larger than the rest and should contribute most to lowering the ground-state energy. Moreover, we find that ADAPT-VQE chooses the same circuit for many contiguous iterations, showing plateaus that indicate a constant number of CNOTs in all but one circuit during various iterations. More details on the specifics of the ADAPT-VQE optimization with EDEF are given in Appendix C, which also gives additional details about the number of CNOT gates in each of the circuits that appear in the EDEF approach.

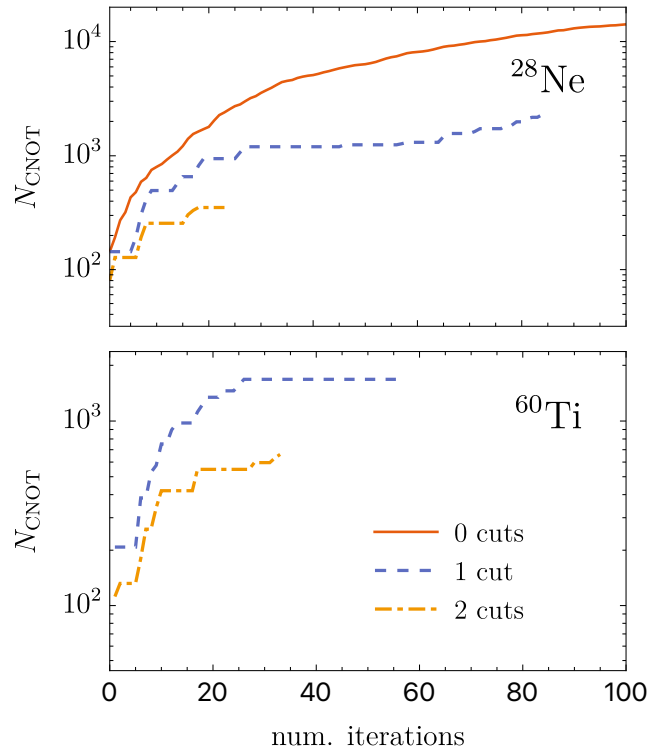


FIG. 8. Number of CNOT gates for the circuit with maximum number for the simulation of ^{28}Ne (top) and ^{60}Ti (bottom) as a function of the ADAPT-VQE iterations. Results for regular ADAPT-VQE (0 cuts, solid red line), EDEF with one layer (1 cut, blue dashed line) and two layers (2 cuts, dashed-dotted yellow lines).

V. SUMMARY AND OUTLOOK

We present a novel procedure, entropy-driven entanglement forging (EDEF), that optimizes the solution of many-body problems in quantum computers using variational quantum algorithms (VQAs). Our approach is based on entanglement forging, which reduces the number of qubits and quantum gates needed to solve the problem. Crucially, in order to decide on the corresponding partitions and coefficients, EDEF adds criteria associated with the entropy between partitions of the system.

With this technique, we have successfully simulated ground states of Fermi-Hubbard (FH) lattices with various central hoppings and interactions, and of the isotopes ^{28}Ne and ^{60}Ti calculated with the nuclear shell model (NSM), in both cases using EDEF with ADAPT-VQE. For these systems, EDEF exploits the low entanglement between the left and right parts of FH lattices or between protons and neutrons in the NSM, and this knowledge is combined with the singular-value degeneracy in the Schmidt decomposition of the ground states. Our EDEF simulations with one layer of EDEF – separating the system in two bipartitions – only need half as many qubits as the regular ADAPT-VQE, and they describe

nuclei with an order of magnitude fewer CNOT gates. Nuclei simulated with two EDEF layers – each bipartition additionally separated into two parts corresponding to higher- and lower-energy single-particle states – need a quarter of the regular ADAPT-VQE qubits and an additional order of magnitude fewer CNOTs.

In terms of performance, in FH lattices EDEF converges better than regular ADAPT-VQE for weak central hopping, and it still works well as long as the central hopping equals the other hoppings, $t_m \approx t$. In the NSM, for ^{28}Ne , one layer of EDEF using 8 circuits is more efficient than the regular ADAPT-VQE, while in ^{26}Ne EDEF performs slightly worse due to the larger proton-neutron entanglement. Furthermore, EDEF allows us to simulate ^{60}Ti , which is beyond our capabilities with the standard ADAPT-VQE. For this nucleus, the two layer EDEF reaches a lower infidelity than the 1-cut EDEF.

In summary, EDEF is ideal to adapting to qubit and CNOT number limitations present in current intermediate-scale noisy devices. In particular, EDEF allows one to adjust the algorithm to produce shallower circuits mitigating the impact of errors. This reduction can be further improved by the adaptability of the trained

parameters expected for a variational algorithm. Furthermore, by reducing the number of qubits EDEF allows one us to use smaller devices with lower error rates. In principle, these advantages can be exploited further by identifying low-entanglement partitions in successive EDEF layers. Beyond the first applications studied in this work, EDEF can optimize other algorithms, as well as other many-body systems for which low-entropy subsystems are identified.

ACKNOWLEDGMENTS

This work is financially supported by MCIN/AEI/10.13039/5011 00011033 from the following grants: PID2020-118758GB-I00, PID2021-127890NB-I00, RYC-2017-22781 and RYC2018-026072 through the “Ramón y Cajal” program funded by FSE “El FSE invierte en tu futuro”, CNS2022-135529 and CNS2022-135716 funded by the “European Union NextGenerationEU/PRTR”, and CEX2019-000918-M to the “Unit of Excellence María de Maeztu 2020-2023” award to the Institute of Cosmos Sciences; and by the Generalitat de Catalunya, grants 2021SGR01095 and 2021SGR00907.

-
- [1] M. Cerezo, A. Arrasmith, R. Babbush, S. C. Benjamin, S. Endo, K. Fujii, J. R. McClean, K. Mitarai, X. Yuan, L. Cincio, P. J. Coles, Variational quantum algorithms, *Nat. Rev. Phys.* 3 (9) (2021) 625–644. doi:10.1038/s42254-021-00348-9.
- [2] J. Tilly, H. Chen, S. Cao, D. Picozzi, K. Setia, Y. Li, E. Grant, L. Wossnig, I. Rungger, G. H. Booth, J. Tenynson, The variational quantum eigensolver: A review of methods and best practices, *Physics Reports* 986 (2022) 1–128. doi:10.1016/j.physrep.2022.08.003.
- [3] A. Anand, P. Schleich, S. Alperin-Lea, P. W. Jensen, S. Sim, M. Díaz-Tinoco, J. S. Kottmann, M. Degroote, A. F. Izmaylov, A. Aspuru-Guzik, A quantum computing view on unitary coupled cluster theory, *Chemical Society Reviews* 51 (2022) 1659–1684. doi:10.1039/D1CS00932J.
- [4] S. McArdle, S. Endo, A. Aspuru-Guzik, S. C. Benjamin, X. Yuan, Quantum computational chemistry, *Rev. Mod. Phys.* 92 (2020) 015003. doi:10.1103/RevModPhys.92.015003.
- [5] M. Haidar, M. J. Rančić, T. Ayrál, Y. Maday, J.-P. Piquemal, Open source variational quantum eigensolver extension of the quantum learning machine for quantum chemistry, *WIREs Computational Molecular Science* 13 (5) (2023) e1664. doi:https://doi.org/10.1002/wcms.1664.
- [6] C. Cade, L. Mineh, A. Montanaro, S. Stanisic, Strategies for solving the fermi-hubbard model on near-term quantum computers, *Phys. Rev. B* 102 (2020) 235122. doi:10.1103/PhysRevB.102.235122.
- [7] A. Pérez-Obiol, A. Pérez-Salinas, S. Sánchez-Ramírez, B. G. M. Araújo, A. García-Saez, Adiabatic quantum algorithm for artificial graphene, *Phys. Rev. A* 106 (2022) 052408. doi:10.1103/PhysRevA.106.052408.
- [8] E. F. Dumitrescu, A. J. McCaskey, G. Hagen, G. R. Jansen, T. D. Morris, T. Papenbrock, R. C. Pooser, D. J. Dean, P. Lougovski, Cloud quantum computing of an atomic nucleus, *Phys. Rev. Lett.* 120 (2018) 210501. doi:10.1103/PhysRevLett.120.210501.
- [9] T. Ayrál, P. Besserve, D. Lacroix, E. A. Ruiz Guzman, Quantum computing with and for many-body physics, *Eur. Phys. J. A* 59 (10) (2023) 227. doi:10.1140/epja/s10050-023-01141-1.
- [10] J. D. Watson, J. Bringewatt, A. F. Shaw, A. M. Childs, A. V. Gorshkov, Z. Davoudi, Quantum Algorithms for Simulating Nuclear Effective Field Theories (2023). arXiv:2312.05344.
- [11] J. Romero, J. P. Olson, A. Aspuru-Guzik, Quantum autoencoders for efficient compression of quantum data, *Quantum Science and Technology* 2 (4) (2017) 045001. doi:10.1088/2058-9565/aa8072.
- [12] T. Parella-Dilmé, K. Kottmann, L. Zambrano, L. Mortimer, J. S. Kottmann, A. Acín, Reducing Entanglement with Physically Inspired Fermion-To-Qubit Mappings, *PRX Quantum* 5 (3) (2024) 030333. arXiv:2311.07409, doi:10.1103/PRXQuantum.5.030333.
- [13] S. Bravyi, G. Smith, J. A. Smolin, Trading classical and quantum computational resources, *Phys. Rev. X* 6 (2016) 021043. doi:10.1103/PhysRevX.6.021043.
- [14] C. Piveteau, D. Sutter, Circuit knitting with classical communication, *IEEE Transactions on Information Theory* 70 (4) (2024) 2734–2745. doi:10.1109/TIT.2023.3310797.
- [15] A. Eddins, M. Motta, T. P. Gujarati, S. Bravyi, A. Mezzacapo, C. Hadfield, S. Sheldon, Doubling the size

- of quantum simulators by entanglement forging, *PRX Quantum* 3 (2022) 010309. doi:10.1103/PRXQuantum.3.010309.
- [16] P. de Schoulepnikoff, O. Kiss, S. Vallecorsa, G. Carleo, M. Grossi, Hybrid ground-state quantum algorithms based on neural schrödinger forging, *Phys. Rev. Res.* 6 (2024) 023021. doi:10.1103/PhysRevResearch.6.023021.
- [17] N. Klco, A. Roggero, M. J. Savage, Standard model physics and the digital quantum revolution: thoughts about the interface, *Rept. Prog. Phys.* 85 (6) (2022) 064301. doi:10.1088/1361-6633/ac58a4.
- [18] A. M. Romero, J. Engel, H. L. Tang, S. E. Economou, Solving nuclear structure problems with the adaptive variational quantum algorithm, *Phys. Rev. C* 105 (2022) 064317. doi:10.1103/PhysRevC.105.064317.
- [19] O. Kiss, M. Grossi, P. Lougovski, F. Sanchez, S. Vallecorsa, T. Papenbrock, Quantum computing of the ${}^6\text{Li}$ nucleus via ordered unitary coupled clusters, *Phys. Rev. C* 106 (2022) 034325. doi:10.1103/PhysRevC.106.034325.
- [20] I. Stetcu, A. Baroni, J. Carlson, Variational approaches to constructing the many-body nuclear ground state for quantum computing, *Phys. Rev. C* 105 (2022) 064308. doi:10.1103/PhysRevC.105.064308.
- [21] C. Sarma, O. Di Matteo, A. Abhishek, P. C. Srivastava, Prediction of the neutron drip line in oxygen isotopes using quantum computation, *Phys. Rev. C* 108 (6) (2023) 064305. doi:10.1103/PhysRevC.108.064305.
- [22] B. Bhoy, P. Stevenson, Shell-model study of ${}^{58}\text{Ni}$ using quantum computing algorithm, *New J. Phys.* 26 (7) (2024) 075001. doi:10.1088/1367-2630/ad5756.
- [23] S. Yoshida, T. Sato, T. Ogata, T. Naito, M. Kimura, Accurate and precise quantum computation of valence two-neutron systems, *Phys. Rev. C* 109 (6) (2024) 064305. doi:10.1103/PhysRevC.109.064305.
- [24] A. Li, A. Baroni, I. Stetcu, T. S. Humble, Deep quantum circuit simulations of low-energy nuclear states, *Eur. Phys. J. A* 60 (5) (2024) 106. doi:10.1140/epja/s10050-024-01286-7.
- [25] A. Pérez-Obiol, A. M. Romero, J. Menéndez, A. Rios, A. García-Sáez, B. Juliá-Díaz, Nuclear shell-model simulation in digital quantum computers, *Scientific Reports* 13 (1) (2023) 12291. doi:10.1038/s41598-023-39263-7.
- [26] J. Tang, R. Xu, Y. Ding, X. Xu, Y. Ban, M. Yung, A. Pérez-Obiol, G. Platero, X. Chen, Exploring ground states of fermi-hubbard model on honeycomb lattices with counterdiabaticity (2024). arXiv:2405.09225.
- [27] R. Horodecki, P. Horodecki, M. Horodecki, K. Horodecki, Quantum entanglement, *Rev. Mod. Phys.* 81 (2009) 865–942. doi:10.1103/RevModPhys.81.865.
- [28] G. Benenti, G. Casati, I. Davide Rossini (Università di Pisa, G. Strini), Entanglement and non-classical correlations, *World Scientific*, 2018, Ch. Chapter 6, pp. 241–286. doi:10.1142/9789813237230_0007.
- [29] M. A. Nielsen, I. L. Chuang, *Introduction to quantum mechanics*, Cambridge University Press, 2010, p. 60–119.
- [30] C. W. Johnson, O. C. Gorton, Proton-neutron entanglement in the nuclear shell model, *J. Phys. G* 50 (4) (2023) 045110. doi:10.1088/1361-6471/acbece.
- [31] A. Pérez-Obiol, S. Masot-Llima, A. M. Romero, J. Menéndez, A. Rios, A. García-Sáez, B. Juliá-Díaz, Quantum entanglement patterns in the structure of atomic nuclei within the nuclear shell model, *The European Physical Journal A* 59 (10) (2023) 240. doi:10.1140/epja/s10050-023-01151-z.
- [32] J. Hubbard, Electron correlations in narrow energy bands, *Proceedings of the Royal Society of London. Series A, Mathematical and Physical Sciences* 276 (1365) (1963) 238–257. doi:10.1098/rspa.1963.0204.
- [33] P. Jordan, E. P. Wigner, Über das paulische äquivalenzverbot, in: *The Collected Works of Eugene Paul Wigner*, Springer, 1993, pp. 109–129.
- [34] A. De-Shalit, I. Talmi, *Nuclear shell theory*, Vol. 14, Academic Press, 2013.
- [35] K. L. Heyde, K. L. Heyde, *The nuclear shell model*, Springer, 1994.
- [36] B. A. Brown, B. H. Wildenthal, Status of the nuclear shell model, *Annu. Rev. Nucl. Part. Sci.* 38 (1) (1988) 29–66. doi:10.1146/annurev.ns.38.120188.000333.
- [37] E. Caurier, G. Martínez-Pinedo, F. Nowacki, A. Poves, A. Zuker, The shell model as a unified view of nuclear structure, *Rev. Mod. Phys.* 77 (2) (2005) 427. doi:10.1103/RevModPhys.77.427.
- [38] T. Otsuka, A. Gade, O. Sorlin, T. Suzuki, Y. Utsuno, Evolution of shell structure in exotic nuclei, *Rev. Mod. Phys.* 92 (2020) 015002. doi:10.1103/RevModPhys.92.015002.
- [39] S. R. Stroberg, S. K. Bogner, H. Hergert, J. D. Holt, Nonempirical interactions for the nuclear shell model: An update, *Ann. Rev. Nucl. Part. Sci.* 69 (2019) 307–362. doi:10.1146/annurev-nucl-101917-021120.
- [40] B. A. Brown, W. A. Richter, New “USD” Hamiltonians for the *sd* shell, *Phys. Rev. C* 74 (2006) 034315. doi:10.1103/PhysRevC.74.034315.
- [41] A. Poves, J. Sánchez-Solano, E. Caurier, F. Nowacki, Shell model study of the isobaric chains $A=50$, $A=51$ and $A=52$, *Nucl. Phys. A* 694 (1) (2001) 157–198. doi:10.1016/S0375-9474(01)00967-8.
- [42] N. Shimizu, T. Mizusaki, Y. Utsuno, Y. Tsunoda, Thick-Restart Block Lanczos Method for Large-Scale Shell-Model Calculations, *Comput. Phys. Commun.* 244 (2019) 372–384. doi:10.1016/j.cpc.2019.06.011.
- [43] E. Caurier, F. Nowacki, Present status of shell model techniques, *Acta Phys. Pol. B* 30 (1999) 705. URL <https://www.actaphys.uj.edu.pl/fulltext?series=Reg&vol=30&page=705>
- [44] B. Brown, W. Rae, The shell-model code NuShellX@MSU, *Nucl. Data Sheets* 120 (2014) 115–118.
- [45] C. W. Johnson, W. E. Ormand, K. S. McElvain, H. Shan, BIGSTICK: A flexible configuration-interaction shell-model code (2018). arXiv:1801.08432.
- [46] C. Robin, M. J. Savage, N. Pillet, Entanglement rearrangement in self-consistent nuclear structure calculations, *Phys. Rev. C* 103 (2021) 034325. doi:10.1103/PhysRevC.103.034325.
- [47] S. M. Hengstenberg, C. E. Robin, M. J. Savage, Multi-body entanglement and information rearrangement in nuclear many-body systems: a study of the lipkin–meshkov–glick model, *The European Physical Journal A* 59 (10) (2023) 231. doi:10.1140/epja/s10050-023-01145-x.
- [48] C. E. P. Robin, M. J. Savage, Quantum simulations in effective model spaces: Hamiltonian-learning variational quantum eigensolver using digital quantum computers and application to the Lipkin-Meshkov-Glick model, *Phys. Rev. C* 108 (2) (2023) 024313. doi:10.1103/

- [PhysRevC.108.024313](#).
- [49] A. Tichai, S. Knecht, A. Kruppa, Ö. Legeza, C. Moca, A. Schwenk, M. Werner, G. Zarand, Combining the in-medium similarity renormalization group with the density matrix renormalization group: Shell structure and information entropy, *Phys. Lett. B* 845 (2023) 138139. [doi:10.1016/j.physletb.2023.138139](#).
- [50] C. Gu, Z. H. Sun, G. Hagen, T. Papenbrock, Entanglement entropy of nuclear systems, *Phys. Rev. C* 108 (5) (2023) 054309. [doi:10.1103/PhysRevC.108.054309](#).
- [51] A. Tichai, K. Kapás, T. Miyagi, M. A. Werner, O. Legeza, A. Schwenk, G. Zarand, Spectroscopy of N=50 isotones with the valence-space density matrix renormalization group, *Phys. Lett. B* 855 (2024) 138841. [doi:10.1016/j.physletb.2024.138841](#).
- [52] O. C. Gorton, C. W. Johnson, Weak entanglement approximation for nuclear structure, *Phys. Rev. C* 110 (3) (2024) 034305. [doi:10.1103/PhysRevC.110.034305](#).
- [53] S. Cohen, D. Kurath, Effective interactions for the 1p shell, *Nucl. Phys.* 73 (1) (1965) 1–24. [doi:10.1016/0029-5582\(65\)90148-3](#).
- [54] H. R. Grimsley, S. E. Economou, E. Barnes, N. J. Mayhall, An adaptive variational algorithm for exact molecular simulations on a quantum computer, *Nat. Commun.* 10 (1) (2019) 1–9. [doi:10.1038/s41467-019-10988-2](#).
- [55] H. L. Tang, V. Shkolnikov, G. S. Barron, H. R. Grimsley, N. J. Mayhall, E. Barnes, S. E. Economou, Qubit-adapt-vqe: An adaptive algorithm for constructing hardware-efficient ansätze on a quantum processor, *PRX Quantum* 2 (2021) 020310. [doi:10.1103/PRXQuantum.2.020310](#).
- [56] P. G. Anastasiou, Y. Chen, N. J. Mayhall, E. Barnes, S. E. Economou, Tetris-adapt-vqe: An adaptive algorithm that yields shallower, denser circuit ansätze, *Physical Review Research* 6 (1) (2024) 013254. [doi:10.1103/PhysRevResearch.6.013254](#).
- [57] M. Ramôa, P. G. Anastasiou, L. P. Santos, N. J. Mayhall, E. Barnes, S. E. Economou, Reducing the resources required by adapt-vqe using coupled exchange operators and improved subroutines, *arXiv preprint arXiv:2407.08696* (2024).
- [58] C. Feniou, M. Hassan, D. Traoré, E. Giner, Y. Maday, J.-P. Piquemal, Overlap-adapt-vqe: practical quantum chemistry on quantum computers via overlap-guided compact ansätze, *Communications Physics* 6 (1) (2023) 192. [doi:https://doi.org/10.1038/s42005-023-01312-y](#).
- [59] Y. S. Yordanov, V. Armaos, C. H. Barnes, D. R. Arvidsson-Shukur, Qubit-excitation-based adaptive variational quantum eigensolver, *Communications Physics* 4 (1) (2021) 228. [doi:https://doi.org/10.1038/s42005-021-00730-0](#).
- [60] H. R. Grimsley, G. S. Barron, E. Barnes, S. E. Economou, N. J. Mayhall, Adaptive, problem-tailored variational quantum eigensolver mitigates rough parameter landscapes and barren plateaus, *npj Quantum Information* 9 (1) (2023) 19. [doi:https://doi.org/10.1038/s41534-023-00681-0](#).
- [61] R. C. Farrell, M. Illa, A. N. Ciavarella, M. J. Savage, Quantum simulations of hadron dynamics in the schwinger model using 112 qubits, *Phys. Rev. D* 109 (2024) 114510. [doi:10.1103/PhysRevD.109.114510](#).
- [62] R. C. Farrell, M. Illa, A. N. Ciavarella, M. J. Savage, Scalable circuits for preparing ground states on digital quantum computers: The schwinger model vacuum on 100 qubits, *PRX Quantum* 5 (2024) 020315. [doi:10.1103/PRXQuantum.5.020315](#).
- [63] S. Baid, A. Sáiz, L. Lamata, P. Pérez-Fernández, A. Romero, A. Ríos, J. Arias, J. García-Ramos, The extended lipkin model: proposal for implementation in a quantum platform and machine learning analysis of its phase diagram (2024). [arXiv:2404.15558](#).
- [64] J. Zhang, D. Lacroix, Y. Beaujeault-Taudiere, Neutron-proton pairing correlations described on quantum computers (8 2024). [arXiv:2408.17294](#).

Appendix A: Initial states and coefficients of EDEF

In the main text we outlined the initial states needed for EDEF. In this section we give extended detail and a few examples for both the first layer and second layer of EDEF.

1. First layer of entanglement forging

For a FH lattice of four sites, we use five pairs of circuits with four qubits, instead of a single circuit with eight qubits. Each circuit simulates a quantum state term in the product of the truncated (and renormalized) Schmidt decomposition:

$$|\psi\rangle = \lambda_0 |l_{\uparrow\downarrow}\rangle \otimes |r_{\uparrow\downarrow}\rangle + \lambda_1 (|l_{\uparrow\uparrow}\rangle \otimes |r_{\downarrow}\rangle + |l_{\downarrow}\rangle \otimes |r_{\uparrow\uparrow}\rangle + |l_{\uparrow\downarrow}\rangle \otimes |r_{\uparrow}\rangle + |l_{\downarrow}\rangle \otimes |r_{\uparrow\downarrow}\rangle). \quad (\text{A1})$$

A single circuit of four qubits, for example, simulates the state $|l_{\uparrow\downarrow}\rangle$ in the first product state, which simulates the left part of the lattice, labeled with l , and which has one spin up fermion and one with spin down, labeled in the subindex as $\uparrow\downarrow$. Note that all states are naturally orthogonal as they involve different distributions of particles and spins. This orthogonality is maintained as operators from the pool, which conserve spin and particle number, are added to each circuit.

For the nuclear shell model and for all isotopes considered, with one layer of entanglement forging we separate the proton and neutrons degrees of freedom as shown in Fig. 4 and thus reduce by half the number of qubits of the simulating circuits. As observed in Fig. 5, the nuclear state can be, to a very good approximation, be approximated using the following truncation in the Schmidt decomposition

$$|\psi\rangle = \lambda_0 |\tilde{p}_0\rangle \otimes |\tilde{n}_0\rangle + \lambda_1 (|p_{-2}\rangle \otimes |n_2\rangle + |p_{-1}\rangle \otimes |n_1\rangle + |p_0\rangle \otimes |n_0\rangle + |p_1\rangle \otimes |n_{-1}\rangle + |p_2\rangle \otimes |n_{-2}\rangle). \quad (\text{A2})$$

With one circuit, for example, we simulate the state $|p_{-2}\rangle$, which corresponds to a superposition of Slater determinants containing only proton orbitals and with expected third component of total angular momentum $\langle p_{-2} | J_z | p_{-2} \rangle = -2$. We need to ensure these states are orthogonal. All states that have different J_z expected

value in each partition are already orthogonal, and will continue to be considering the operators in our pool, but this is not the case for $|\tilde{p}_0\rangle \otimes |\tilde{n}_0\rangle$ and $|p_0\rangle \otimes |n_0\rangle$. For these, we start with different (orthogonal) Slater determinants, $|\psi_0\rangle$, $|\tilde{\psi}_0\rangle$, and then apply the same unitaries to both states to keep them orthogonal, that is, $\langle \tilde{\psi}_0 | e^{-i\theta T} e^{i\theta T} | \psi_0 \rangle = \langle \tilde{\psi}_0 | \psi_0 \rangle = 0$.

At each iteration the gradients are computed for each of the terms in Eqs. (13) and (14) separately, except for $|\tilde{p}_0\rangle \otimes |\tilde{n}_0\rangle$ and $|p_0\rangle \otimes |n_0\rangle$, as they both have the same parameters. In this case $|\psi_c\rangle$ in Eq. (10) represents $\lambda_0 |\tilde{p}_0\rangle \otimes |\tilde{n}_0\rangle + \lambda_1 |p_0\rangle \otimes |n_0\rangle$. Once all the gradients are computed, the largest one determines which operator from the pool is chosen and in which circuit is implemented. To compute the energy, we extract the statevector from each circuit, make the corresponding tensor products between proton and neutron states, add them up as in Eq. (14), and compute the expected value of the Hamiltonian with the obtained statevector. The energy computation in an actual quantum computer could be implemented as proposed in [25], with the exception of crossed statistics in the two non-orthogonal states.

We also notice that, considering the normalization of the truncated state, we only have one free parameter λ . We can include λ as another parameter in the optimizer when classically finding the minimum of the energy surface. In this work, we fix λ to the value given by the Schmidt decomposition, to speed up testing of entanglement forging and focus on the VQE part. Degenerate states are also related by symmetry. For the FH decomposition, Eq. (13), the four degenerate states are related by spin and parity transformations. Therefore, only two independent product states and four circuits need to be optimized, for example $|l_{\uparrow\downarrow}\rangle \otimes |r_{\uparrow\downarrow}\rangle$ and $|l_{\uparrow\downarrow}\rangle \otimes |r_{\downarrow\uparrow}\rangle$. Similarly, the five degenerate product states in Eq. (14) are related by parity. Slater determinants with same angular momentum j and opposite m satisfy $|j, m\rangle = (-1)^{j-m} |j, -m\rangle$, with $|j, m\rangle \equiv a_{j,m}^\dagger |0\rangle$. We can then simulate only $|p_{-2}\rangle \otimes |n_2\rangle$, $|p_{-1}\rangle \otimes |n_1\rangle$, $|p_0\rangle \otimes |n_0\rangle$, and obtain $|p_1\rangle \otimes |n_{-1}\rangle$, $|p_2\rangle \otimes |n_{-2}\rangle$ through a parity transformation. Thus we need a total of four product states and eight circuits.

2. Second layer of entanglement forging

For the FH model, we do not consider a second layer of entanglement forging as there is no clear partition to take advantage of, and the effects of the barrier can be properly studied with just the first layer.

We can apply the same procedure to each of the circuits simulating states with only proton or neutron orbitals, and consequently use circuits with one fourth as many qubits as orbitals there are in the shell. As a second decomposition we choose to split each proton and neutron partition into low and high energy subshells. In the case of the sd -shell, the bottom half consists of the lowest subshell, $0d_{5/2}$, while the upper half includes sub-

shells $1s_{1/2}$ and $0d_{3/2}$. For the pf -shell, this second cut involves splitting the subshell $1p_{3/2}$ in half, as shown in Fig. 4.

This division is useful to test our approach beyond one-cut, but it is not as good as the proton-neutron separation in terms of entropy. Ideally, physical systems that exhibit more sectors with low entanglement would be better suited for a larger amount of cuts, including divisions into t circuits instead of successive cuts in 2. Also, in contrast to the first decomposition, where we have degenerate Schmidt coefficients for product states with well defined spin J_z and isospin T_z , in this second decomposition we are free to choose the particular distribution of product states. In this case we decompose each product state into states with a different particle number distribution between the bottom and top orbitals. For example, if we have two valence protons, we can have both protons in the bottom subshells and none in the others, labeled as (2,0), one in each partition, (1,1), or both protons in the upper subshells, (0,2). These are all the possibilities to distribute the protons in all the neon and titanium isotopes. For ^{28}Ne and ^{60}Ti we have 10 and 18 valence neutrons respectively, implying two holes in both nuclei. We can distribute these holes as (0,2), (1,1) and (2,0).

To add only few more parameters to the ansatz we decompose each of the previous statevectors with well defined spin and isospin into only two terms with different particle distributions. For the first term in Eq. 14, with $S_z^{(p)} = S_z^{(n)} = 0$ and labeled $|\psi_{00}\rangle$, we consider two terms with a symmetric distribution of protons in the lower and higher energy orbitals, of (2,0) and (0,2). For the corresponding neutron states, the distribution of neutron holes is (0,2) and (2,0),

$$\begin{aligned} |\psi_{00}\rangle &\equiv \lambda_0 |\tilde{p}_0\rangle \otimes |\tilde{n}_0\rangle \\ &= (b_1 |p_{20}\rangle + b_2 |p_{02}\rangle) \otimes (b'_1 |n_{20}\rangle + b'_2 |n_{02}\rangle) \\ &= \left(b_1 |p_2^{(b)}\rangle \otimes |p_0^{(t)}\rangle + b_2 |p_0^{(b)}\rangle \otimes |p_2^{(t)}\rangle \right) \\ &\quad \otimes \left(b'_1 |n_0^{(b)}\rangle \otimes |n_2^{(t)}\rangle + b'_2 |n_2^{(b)}\rangle \otimes |n_0^{(t)}\rangle \right). \end{aligned} \quad (\text{A3})$$

In the other five states, we assume a distribution of (2,0), (1,1) for protons, and (0,2), (1,1) for neutron holes. That is, the most energetically favorable one.

Considering two terms also allows to not have to impose a normalization condition, since one of the coefficients is determined by the other. We only impose bounds on b_1, b_2 such that these coefficients can be normalized to λ_0 or λ_1 , which are again fixed to the values given by the Schmidt decomposition. For example, $\sqrt{b_1^2 + b_2^2} = \sqrt{\lambda_0}$, and the same for the normalization of $|n_0\rangle$, $\sqrt{b'_1{}^2 + b'_2{}^2} = \sqrt{\lambda_0}$ such that their product is normalized to λ_0 . This also displays the training procedure for the coefficients that we propose for general use.

In Appendix C we show other more technical improvements in the optimization of ^{60}Ti , which go beyond splitting the circuits into halves and fourths and which allow to speed up the simulation.

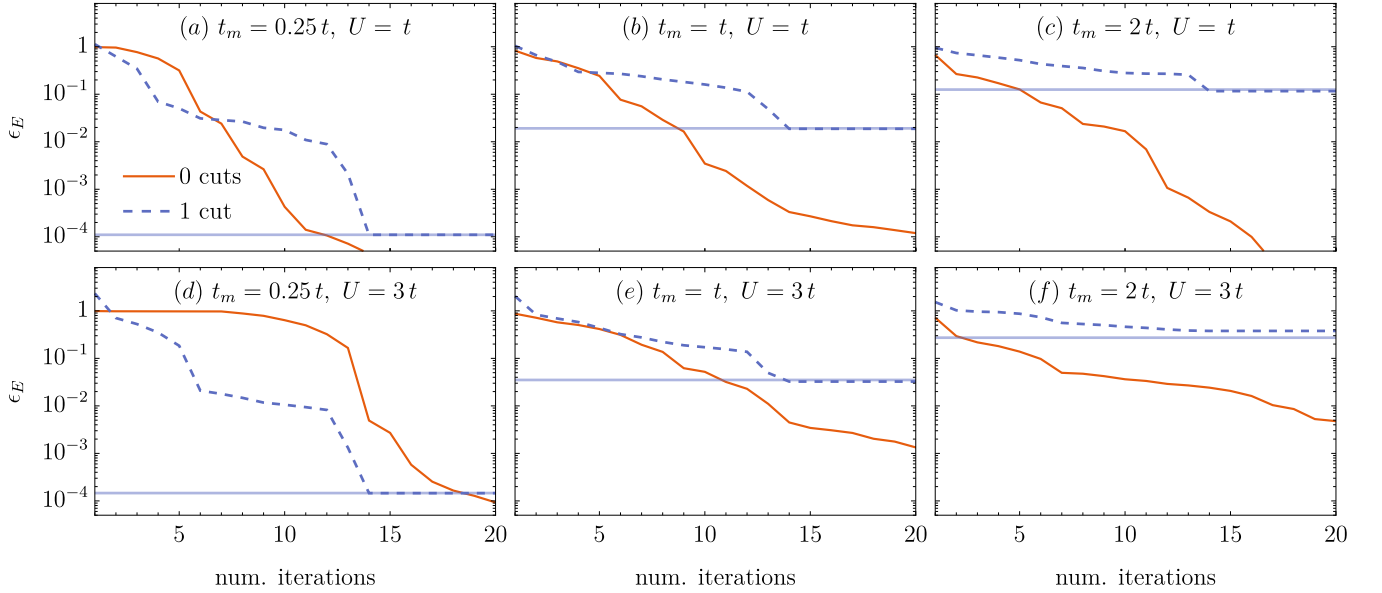


FIG. 9. Relative errors in energy ϵ_E for the same FH simulations with interaction U , middle hopping t_m pairs and "cuts" as shown in Fig. 6. Horizontal lines mark the errors ϵ_E determined by the corresponding Schmidt decompositions of the given layer (lower blue line). These errors can also be seen to decrease substantially as t_m and entanglement diminish.

Appendix B: Further details on the convergence of EDEF in the nuclear shell model

In the main text we showed the convergence of the infidelity in our examples as the most appropriate metric to test the method. The training, however, is based on minimizing the energy. For this reason, we also include here the relative errors in the energy, ϵ_E , as the iterations of the optimization progress. Namely, in Fig. 9 we show the counterpart to Fig. 6, and in Fig. 10 the counterpart to Fig. 7. We can see that in both physical systems the behaviour of this error is qualitatively the same as that of infidelity, commented on the main text. In this case, relative energy errors given by the corresponding Schmidt decompositions, marked with horizontal lines, do not define a lower bound. In fact, for the ^{28}Ne 1-cut EDEF simulation, the converged ϵ_E is slightly lower than its corresponding Schmidt decomposition ϵ_E .

We also extend the amount of detail in the CNOT counts, N_{CNOT} , by taking into account the effect of each subcircuit. Fig. 11 shows the number of CNOTs for regular ADAPT-VQE (solid black line on the top of the plot), together with N_{CNOT} for each circuit in the simulation with one layer of entanglement forging. N_{CNOT} for all 1-cut EDEF circuits are notably lower throughout all the evolution. Within single-cut EDEF lines we distinguish two-scales, $N_{\text{CNOT}} \simeq 2 \times 10^3$ for subcircuits simulating the first product state, with largest singular value, and $N_{\text{CNOT}} \lesssim 10^3$ for the rest of subcircuit.

In Fig. 12 we show similarly the CNOT counts for all subcircuit with 2-cut EDEF. The leading circuit is the neutron state with $S_z = 0$.

The simulations of ^{60}Ti show similar results to ^{28}Ne

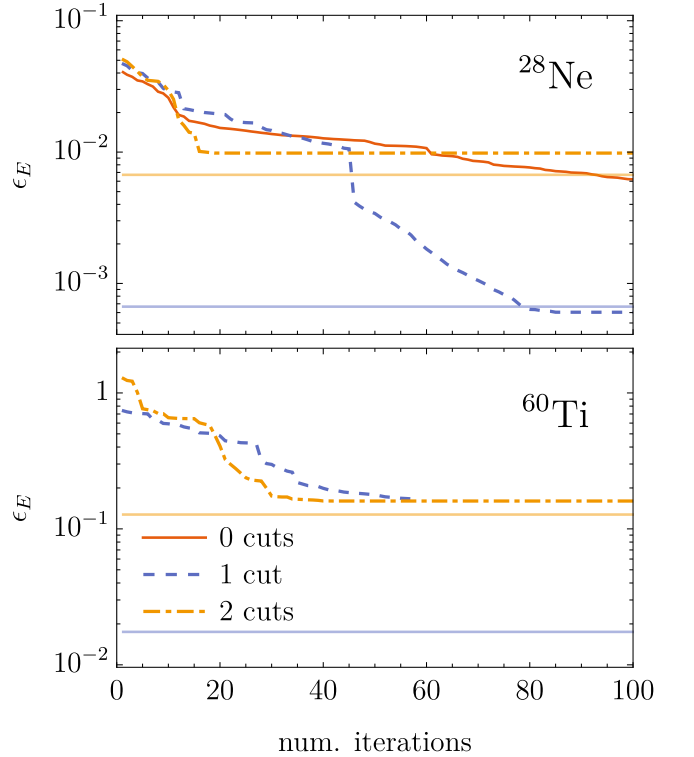


FIG. 10. Relative errors in ground state energy for ^{28}Ne (top panel) and ^{60}Ti (bottom pane) as a function of the number of ADAPT-VQE iterations for 0-, 1-, and 2-cuts EDEF simulations.

in terms of number of CNOTs. Specifically, ^{60}Ti with

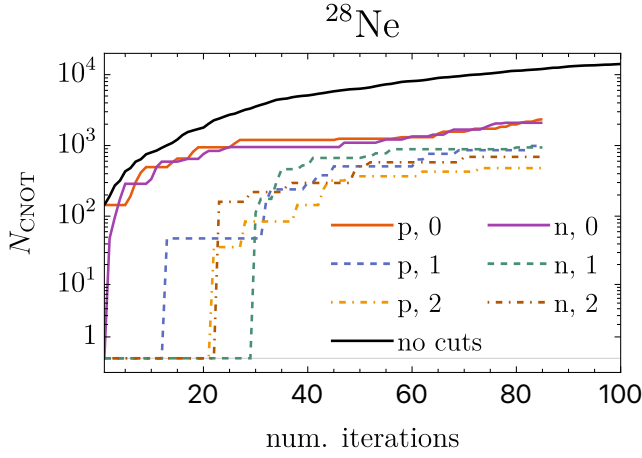


FIG. 11. CNOT count in each circuit for the simulation of ^{60}Ti as function of ADAPT-VQE iterations for one cut.

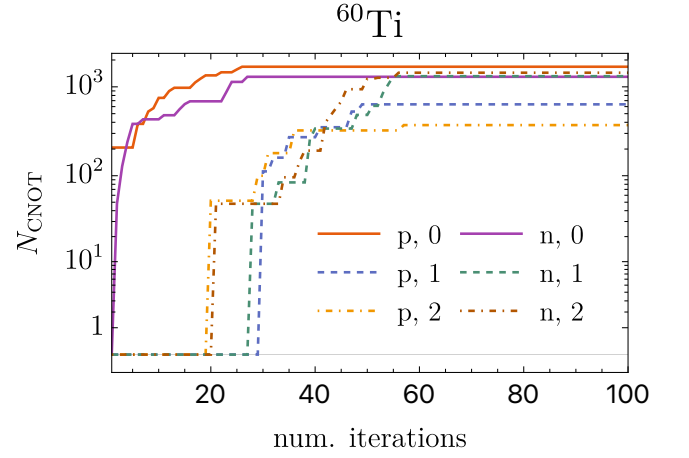


FIG. 13. CNOT count in each circuit for the simulation of ^{60}Ti as function of ADAPT-VQE iterations for one cut.

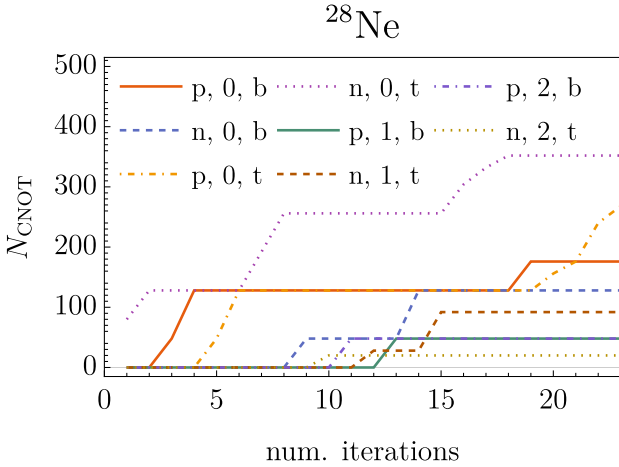


FIG. 12. CNOT count in each circuit for the simulation of ^{60}Ti as function of ADAPT-VQE iterations for one cut.

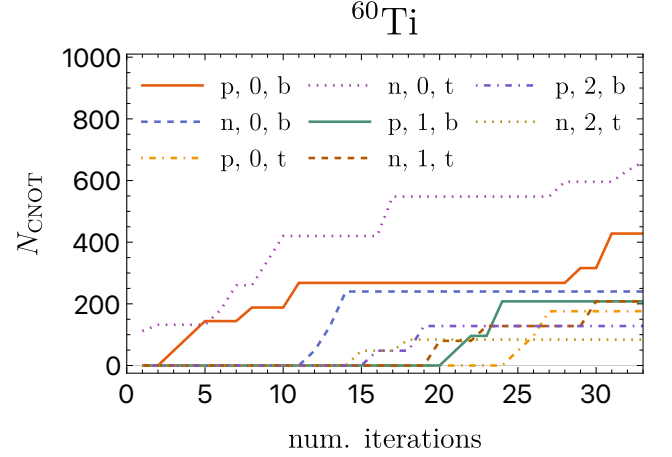


FIG. 14. Number of CNOTs in each circuit for ^{60}Ti as function of ADAPT-VQE iterations for two cuts.

one cut also shows a large difference between N_{CNOT} for $S_z = 0$ and $S_z = 1, 2$ circuits. The former are of the order of 10^3 for each proton and neutron circuits after 40 iterations, where ADAPT-VQE is not yet converged, see Fig. 13. This is similar to the neon isotopes, where ADAPT-VQE chooses in most of the iterations to apply an operator to one of the circuits corresponding to the first product state.

CNOT counts for ^{60}Ti with two cuts are plotted in Fig. 14. The circuits with most CNOTs are much shallower than 1-cut ADAPT-VQE with the same number of iterations. In this case circuit with largest N_{CNOT} is the one for neutrons with $S_z = 0$ corresponding to the top subshells, which contains 660 CNOTs.

Finally, in the main text we briefly mentioned how results of ^{28}Ne compare to those of ^{26}Ne , as an example with less particle/hole symmetry than the simulations in the main text, but for which the first layer of entanglement forging also performs well. We include here such

simulation for completeness.

We plot the same errors as in section IV B for 0- and 1-cuts simulations for ^{26}Ne in Fig. 15 with solid red and dashed blue lines, respectively. In this case both lines have a very similar behaviour, decreasing gradually down to $\epsilon_E = 0.013$, $I = 0.11$, for 0 cuts, and to $\epsilon_E = 0.016$, $I = 0.16$ for 1 cut. Neither ADAPT-VQE has converged into a local minimum at the 100th iteration, and in the case of 1-cut ADAPT-VQE, the infidelity and errors are still well above the values obtained from the decomposition of the exact solution into six product states, $\epsilon_E^{(1)} = 0.011$ and $I^{(1)} = 0.044$.

Appendix C: Optimization improvements

The implementation of a variational algorithm such as ADAPT-VQE can fall short even when the ansatz and

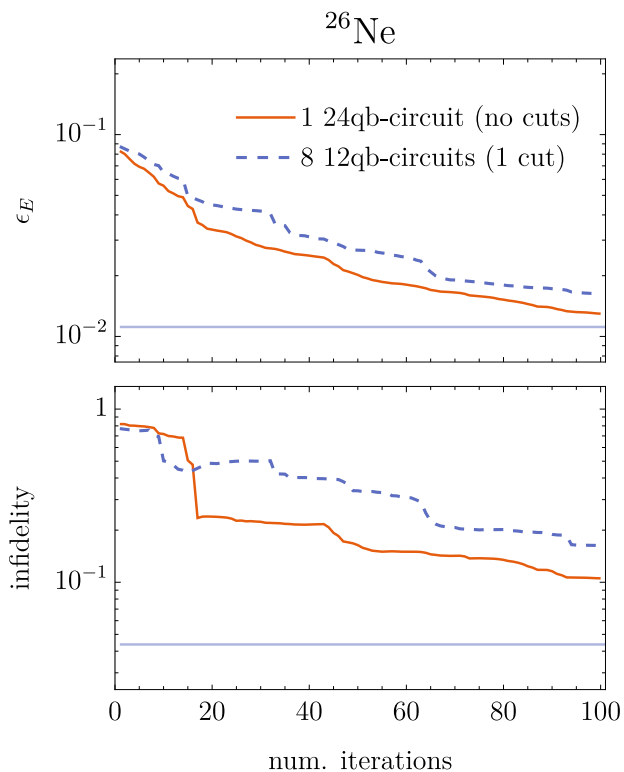


FIG. 15. ϵ_E (top plot) and I (bottom plot) for ^{26}Ne as a function of the number iterations for 0 and 1 cuts.

operator pool are adequate for the physical problem due to the necessity of training the parameters. Different implementations of the gradient descent work better for specific problems, but in general they will all run into resource problems as we try to deal with bigger systems. In this section, we present some optimization techniques that we implemented to increase the size of simulatable systems given a specific resource budget, and were specially useful to extend the simulation of the ^{60}Ti nucleus into more layers.

Firstly, the more expensive step is often the parameter tuning. However, the parameters found after the

update are in general quite close to the previous step. Instead of optimizing over all parameters each time, one can find the optimal parameter only for the last operator that was added, and perform a complete update of all parameters every l rounds. Because now the operator with the biggest gradient is found with different parameters, the list of chosen operators may vary from the usual approach (equivalent to $l \neq 1$), making l a hyperparameter l that needs tuning. Despite this, we found that the precision of the training after the same amount of steps was close with high probability, even with a different set of chosen operators – this is consistent with the fact that the same ground state can be reached with different compositions of unitaries, due to non-uniqueness of unitary decomposition. While performance increases with l , one cannot make it too large because with fixed parameters, even if close to the optimal value, the error can only be decreased by adding extra operators, and a deep circuit becomes exponentially expensive to simulate.

In our entanglement forging approach to ADAPT-VQE, we find that the main circuit, the one with the leading coefficient on the Schmidt decomposition, is often prioritized by the operator choice. As we have mentioned, deep circuits are harder to simulate, so one can exhaust the resources available by always choosing the optimal operator even if some of the subleading circuits are almost empty. If we sometimes choose to place an operator in a circuit that is shallow (and therefore easy to compute), we can improve our error with a relatively inexpensive step (specifically, relative to the progress in the algorithm). In addition, since gradients are evaluated at a fixed point and the optimization happens over all parameter space, the error can decrease more on a single step by adding operators that have a non-optimal gradient. This makes this technique have an even bigger impact, as some of these steps will be more efficient and also more effective. We implemented this idea by excluding the “full” circuit from the choice of operators. This was done with an ad-hoc heuristic based on the optimization duration in the specific setup used, but can also be generalized into an hyperparameter φ .